GEOPHYSICS, VOL. 78, NO. 6 (NOVEMBER-DECEMBER 2013); P. D403–D418, 16 FIGS., 3 TABLES.
10.1190/GEO2013-0100.1

Complex conductivity tensor of anisotropic hydrocarbon-bearing shales and mudrocks

A. Revil[1], W. F. Woodruff[2], C. Torres-Verdín[3], and M. Prasad[4]

ABSTRACT

A model was recently introduced to describe the complex electrical conductivity and high-frequency dielectric constant of isotropic clayey porous materials. We generalized that approach to the case of anisotropic and tight hydrocarbon-bearing shales and mudrocks by introducing tensorial versions of formation factor and tortuosity. In-phase and quadrature conductivity tensors have common eigenvectors, but the eigenvectors of the dielectric tensor may be different due to influence of the solid phase at high frequencies. In-phase and quadrature contributions to complex electrical conductivity depend on saturation, salinity, porosity, temperature, and cation exchange capacity (alternatively, specific surface area) of the porous material. Kerogen is likely to have a negligible contribution to the cation exchange capacity of the material because all exchangeable sites in the functional groups of organic matter may have been polymerized during diagenesis. An anisotropic experiment is performed to validate some of the properties described by the proposed model, especially to verify that the electrical anisotropy factor is the same for in-phase and quadrature conductivities. We used two samples from the Bakken formation. Experimental data confirm the validity of the model. Also, the range of values for cation exchange capacity determined when implementing the new model with experimental data agree with the known range of cation exchange capacity for the Bakken shale. Measurements indicate that the bulk-space tortuosity in the direction normal to bedding plane can be higher than 100.

INTRODUCTION

Shale formations are of increasing interest in hydrocarbon exploration worldwide. They comprise a diverse set of rock types, but are generally characterized as fine-grained, low-porosity, and low-permeability rocks, with a nonnegligible clay fraction in terms of bulk petrophysical properties. Due to preferential orientation of mineral foliations and finely laminated bedding planes, shales and mudrocks are almost ubiquitously anisotropic in several of their macroscopic physical properties. The term mudrock is used to describe all fine-grained shaly and nonshaly formations. It is of great interest to petrophysicists to develop new models to describe seismic and electromagnetic (EM) measurements in these anisotropic materials.

Oil-shale deposits correspond to immature, organic-rich source rocks resulting in high kerogen mass fractions due to limited burial and thermal maturation histories–effectively, they have not been heated sufficiently to release their hydrocarbons. Hence, oil shales and mudrocks are typically water-wet, single- or dual-phase fluid systems, characterized by a heterogeneous solid phase comprising siliciclastic, carbonate, and organic components. Mudrock-oil formations involve complex multiphase fluid systems, in which the degradation of kerogen, through geochemical thermal maturation processes (i.e., catagenesis and metagenesis), has altered the nature of the solid fraction and produced economically significant polar and nonpolar, aromatic and hydrocarbon fluid fractions. Oil-shale and shale-oil deposits represent two generalized regimes in the continuum of shale thermal maturation, exhibiting measurable differences in the characteristics of both solid and fluid phases. In what follows, we refer to all these rock formations in a general manner as shales, tacitly implying that their properties are intrinsically related to the maturation history of each formation. Note, however, that

Manuscript received by the Editor 9 March 2013; revised manuscript received 10 May 2013; published online 3 October 2013.
[1]Colorado School of Mines, Department of Geophysics, Golden, Colorado, USA and Université de Savoie, ISTerre, Le Bourget du Lac, France. E-mail: arevil@mines.edu.
[2]Colorado School of Mines, Department of Geophysics, Golden, Colorado, USA. E-mail: wfwoodruff@gmail.com.
[3]University of Texas at Austin, Department of Petroleum and Geosystems Engineering, Austin, Texas, USA. E-mail: cverdin@austin.utexas.edu.
[4]Colorado School of Mines, Department of Petroleum Engineering, Golden, Colorado, USA. E-mail: mprasad@mines.edu.

mudrocks is a geologically more appropriate term to use because that term does not specify any lithology; rather it denotes a fine-grained rock system.

There is a growing need to better characterize the so-called "sweet spots" of tight oil-mudrock formations using an arsenal of geophysical methods with the objective to optimize hydrocarbon detection and production. Among such methods, galvanic and electromagnetic (EM) measurements can be used to determine the complex electrical conductivity of formations through borehole and cross-well imaging. What is missing is a generally effective complex electrical conductivity model specific for shales and mudrocks, which includes the relative effects of porosity, water saturation, kerogen content and type, clay content and type, and a tortuosity tensor describing the anisotropy of the material (generally expected to be transversely isotropic, [TI]). As discussed in Revil (2013a, 2013b), such a model should also include the description of the high-frequency permittivity of the material and possibly Maxwell-Wagner polarization. Recent developments in logging technology now allow one to resolve the macroscopic effects of anisotropy. Despite progresses on the experimental front (e.g., Weller et al., 2010), robust theoretical models describing the full effective complex conductivity tensor are still lacking (Bittar et al., 2009).

Revil and colleagues (Leroy et al., 2008; Leroy and Revil, 2009; Revil and Florsch, 2010) invoke a strong role of the Stern layer (the inner portion of the electrical double layer coating the surface of mineral grains) to explain the low-frequency polarization of mixed, sandy, and clayey materials. The model of Stern-layer polarization appears to be reliable to explain the dependence of complex electrical conductivity on cation exchange capacity (CEC) and specific surface area (Revil, 2012, 2013a), salinity (Revil and Skold, 2011; Weller and Slater, 2012), pH (Skold et al., 2011), sorption of cations and organic molecules (Vaudelet et al., 2011a, 2011b; Schwartz and Furman, 2012), influence of grain size (Revil et al., 2012), the relationship between surface conductivity and quadrature conductivity (Revil and Florsch, 2010; Revil, 2012; 2013b), temperature (Zisser et al., 2010a), and water saturation (Schmutz et al., 2010; Revil et al., 2012; Revil, 2013a). Here, we generalize this model to the case of anisotropic formations with the intent to quantify the role played by kerogen on surface conductivity and quadrature conductivity. Beside the contribution of the electrical double layer of nonconducting minerals, there is also a strong role played by the presence of pyrite above oil reservoirs (e.g., Veeken et al., 2009) and in the shallow subsurface associated with the biochemistry of contaminant plumes (Flores Orozco et al., 2011). Pyrite plays an active role in spectral induced polarization as long as its surface has not been oxidized. In addition, with the exception of the work by Zisser and Nover (2009) and Zisser et al. (2010b), there are a few open publications documenting and or explaining the polarization and anisotropy of tight (low-permeability) porous rocks.

THE ISOTROPIC CASE AND ITS GENERALIZATION

Ampère's law in isotropic media

Let $\omega = 2\pi f$ designate angular frequency and $f = \omega/(2\pi)$ linear frequency (in hertz). For isotropic materials, Ampère's law is written as (e.g., Vinegar and Waxman, 1984)

$$\nabla \times \mathbf{H} = [\sigma_{\text{eff}} - i\omega\varepsilon_{\text{eff}}]\mathbf{E}, \tag{1}$$

$$\sigma_{\text{eff}} = \sigma'(\omega) + \omega\varepsilon''(\omega), \tag{2}$$

and

$$\varepsilon_{\text{eff}} = \varepsilon'(\omega) - \frac{\sigma''(\omega)}{\omega}, \tag{3}$$

where $\mathbf{H}$ and $\mathbf{E}$ denote magnetic and electrical fields, respectively, $i = \sqrt{-1}$ denotes the pure imaginary number, and σ' and σ'' (expressed in S m^{-1}) denote the real (in-phase) and imaginary (out-of-phase or quadrature) components of the complex conductivity σ^*, respectively, and are given by

$$\sigma* = \sigma' + i\sigma'' = |\sigma| \exp(i\varphi), \tag{4}$$

with the magnitude of the conductivity written as $|\sigma^*| = (\sigma\prime^2 + \sigma\prime\prime^2)^{1/2}$ and the phase lag φ given by $\tan\varphi = \sigma''/\sigma'$. In the frequency range 0.1–1000 Hz, in-phase and quadrature conductivities are only slightly frequency-dependent because grain polarization occurs over a broad range of scales (Vinegar and Waxman, 1984; Revil, 2012, 2013a, 2013b). Complex permittivity is written as $\varepsilon^* = \varepsilon' + i\varepsilon''$. By neglecting the polarization of water molecules (above 1 GHz) and Maxwell-Wagner polarization, one can safely neglect the imaginary component of the dielectric constant, whereby $\varepsilon^* \approx \varepsilon'$, thus giving rise to the approximation $\sigma_{\text{eff}} \approx \sigma'(\omega)$.

In-phase conductivity

Revil (2013a, 2013b) developed a new model to describe the complex conductivity of clayey materials using a volume-average approach. According to Revil (2013a), and assuming volumetric averaging to describe effective conductivity, the in-phase conductivity σ' (in S m^{-1}) of porous materials is given as a function of pore water conductivity σ_w (in S m^{-1}) by the expression

$$\sigma' = \frac{1}{F}\left\{S_w^n\sigma_w + S_w^p\left(\frac{F-1}{F\phi}\right)\rho_S[\beta_{(+)}(1-f) + \beta_{(+)}^S f]\text{CEC}\right\}, \tag{5}$$

where F (dimensionless) denotes the (intrinsic) formation factor for resistivity. It is related to connected porosity ϕ by Archie's equation $F = \phi^{-m}$ where m (dimensionless) denotes the porosity exponent. The total connected porosity entering Archie's law does not distinguish between kerogen and matrix porosities. The parameters n and p (both dimensionless) denote the second Archie exponent (saturation exponent) and the saturation exponent for surface conductivity, respectively (with $p = n - 1$ as introduced by Vinegar and Waxman [1984] and demonstrated by Revil [2013a], using a volume-averaging approach), f denotes the fraction of counterions in the Stern layer (see Leroy et al. [2008] and Revil [2012], for discussion for sand and clayey materials), ρ_S denotes mass density of the solid phase (typically $2650 \pm 50\ \text{kg m}^{-3}$ for the crystalline framework of clay minerals), $\beta_{(+)}$ is the mobility of counterions in the diffuse layer, and $\beta_{(+)}^S$ is the mobility of counterions in the Stern layer (both in $\text{m}^2\,\text{s}^{-1}\,\text{V}^{-1}$). For clay minerals, the mobility of counterions in the diffuse layer is equal to the mobility of the same counterions in bulk pore water (e.g., $\beta_{(+)}(\text{Na}^+, 25°\text{C}) = 5.2 \times 10^{-8}\ \text{m}^2\,\text{s}^{-1}\,\text{V}^{-1}$, see Revil, 2012). Mobility of counterions in the Stern layer is substantially smaller and equal to

$\beta^S_{(+)}(25°\mathrm{C}, \mathrm{Na}^+) = 1.5 \times 10^{-10}\ \mathrm{m^2\,s^{-1}\,V^{-1}}$ for clay minerals (Revil, 2012, 2013a, 2013b). The acronym CEC (expressed in $\mathrm{C\,kg^{-1}}$) denotes cation exchange capacity of the material. In equation 5, S_w denotes saturation of the water phase ($S_w = 1$ for a water-saturated material).

Because the formation factor is generally much higher than unity for tight formations ($F \gg 1$), equation 5 can be written as

$$\sigma' \approx \frac{1}{F} S_w^n \sigma_w + S_w^p \left(\frac{1}{F\phi}\right) \rho_S [\beta_{(+)}(1-f) + \beta^S_{(+)} f]\mathrm{CEC}. \tag{6}$$

The second additive term in this last equation corresponds to the surface conductivity σ_S. Equation 6 is also very close to the equation proposed by Revil et al. (1996) (their equation 15) for water-saturated doleritic core samples from the oceanic crust. A simple generalization of the above expression to anisotropic media yields the following expression for the in-phase conductivity tensor

$$\boldsymbol{\sigma}' = \boldsymbol{\sigma}'_{ij} \mathbf{x}_i \otimes \mathbf{x}_j, \tag{7}$$

$$\mathbf{F} = \mathbf{F}_{ij} \mathbf{x}_i \otimes \mathbf{x}_j, \tag{8}$$

$$\mathbf{T} = T_{ij} \mathbf{x}_i \otimes \mathbf{x}_j, \tag{9}$$

and

$$\sigma'_{ij} \approx F_{ij}(S_w^n \sigma_w) + T_{ij} S_w^p \rho_S [\beta_{(+)}(1-f) + \beta^S_{(+)} f]\mathrm{CEC}, \tag{10}$$

where $\mathbf{x}_i (i = 1, 2, 3)$ denote the basis vectors of the Cartesian frame of reference ($\mathbf{x}_i \cdot \mathbf{x}_j = \delta_{ij}$ where δ_{ij} denotes the Kronecker delta), $\mathbf{a} \otimes \mathbf{b}$ represents the tensorial product between vectors $\mathbf{a}$ and $\mathbf{b}$, F_{ij} denotes the components of the (symmetric second-rank) formation factor tensor for the conductivity $\mathbf{F}$, and T_{ij} denotes the components of the (symmetric second-rank) tortuosity tensor of the pore space $\mathbf{T}$. We designate $\mathbf{T}$ as a connectivity tensor, because its entries vary between 0 and 1 and represent the inverse of the tortuosity defined in the isotropic case (see Bear, 1988; Bear and Bachmat, 1991; Bear and Cheng, 2010). Usually, in clayey materials, one has $\beta_{(+)}(1-f) \gg \beta^S_{(+)} f$ (Revil, 2012, 2013a) whereby the last term of equation 10 can be further simplified to $T_{ij} S_w^p \rho_S \beta_{(+)}(1-f)\mathrm{CEC}$. Our model also assumes that the saturation exponent remains more or less the same in different directions. We will see later that this assumption agrees well with the experimental data.

The components of the conductivity formation tensor and connectivity tensor are related to each other by

$$F_{ij} = T_{ij}\phi. \tag{11}$$

Therefore, conductivity formation factor and connectivity tensors share the same eigenvectors and, for the case of TI materials, the anisotropy ratio should be the same for bulk and surface conductivities. This important technical point will be experimentally verified in the last section of the present paper. In the isotropic case, one has

$$F_{ij} = (1/F)\delta_{ij}, \tag{12}$$

whereby

$$T_{ij} = (1/F\phi)\delta_{ij}. \tag{13}$$

Note that the tortuosity τ of the pore space in the isotropic case ($\tau \geq 1$) is defined as (e.g., Pride, 1994; Zhang and Knackstedt, 1995; Clennell, 1997; Sevostianova et al., 2010; Zhang and Sherer, 2012)

$$F = \frac{\tau}{\phi}, \tag{14}$$

$$\tau = F\phi = \phi^{1-m}, \tag{15}$$

where we have used Archie's equation ($F = \phi^{-m}$ with m designating the porosity exponent, Archie, 1942). The isoconductivity point designates the point characterized by a macroscopic conductivity equal to the pore water conductivity (e.g., Revil et al., 1998). Above the isoconductivity point, surface and quadrature conductivity share the same bulk tortuosity, as discussed, for instance, by Revil and Glover (1997); the reason is the following: above the isoconductivity point, surface conductivity is only a perturbation to the pore water conductivity and the electrical field is controlled by the conductivity of the pore space (see discussion in Bernabé and Revil, 1995; Revil and Glover, 1997). Such a behavior explains why the same tortuosity is applied to the bulk and surface conductivities in the "high-salinity" regime. When surface conductivity dominates, conductivity is controlled by the distribution of surface conductance, and the tortuosity of electrical current along the surface of the minerals is different (usually higher) from that in pore water (see Bernabé and Revil, 1995, for a pore network modeling of this effect).

Quadrature conductivity

The expression for quadrature conductivity obtained by Revil (2013a) is

$$\sigma'' \approx S_w^p \left(\frac{1}{F\phi}\right) \rho_S \beta^S_{(+)} f\mathrm{CEC}. \tag{16}$$

We emphasize that the explicit dependence of quadrature conductivity on the inverse of the product $(F\phi)$ and on water saturation raised to the power $p = n - 1$ are consistent with findings by Vinegar and Waxman (1984) and Revil (2013a). However, equation 16 is based on a volume-averaging procedure, whereas Vinegar and Waxman's (1984) model is predominantly based on empirical considerations. Equation 16 agrees with Vinegar and Waxman's (1984) observations in the laboratory (see also Revil [2012, 2013a, 2013b] for some tests using additional data sets). Field observations also confirm an effect of oil saturation upon quadrature conductivity (e.g., Olhoeft, 1986; Deceuster and Kaufmann, 2012).

The generalization of equation 16 to anisotropic media is straightforward, namely,

$$\boldsymbol{\sigma}'' = \sigma''_{ij} \mathbf{x}_i \otimes \mathbf{x}_j, \tag{17}$$

and

$$\sigma''_{ij} = T_{ij} S_w^p \rho_S \beta^S_{(+)} f_M \mathrm{CEC}, \tag{18}$$

where $\boldsymbol{\sigma}''$ denotes the complex conductivity tensor and σ''_{ij} identifies the entries of this tensor. Our model also assumes that the p-exponent remains more or less the same in different directions like for the saturation exponent. We will see later that this assumption agrees well with the experimental data.

The complex conductivity tensor is defined as

$$\boldsymbol{\sigma}^* = \sigma^*_{ij} \mathbf{x}_i \otimes \mathbf{x}_j, \tag{19}$$

and

$$\sigma^*_{ij} = \sigma'_{ij} + i\sigma''_{ij}, \tag{20}$$

where σ'_{ij} and σ''_{ij} are given by equations 10 and 18, respectively.

Dielectric constant

The remaining component of the generalized model is the (true or high-frequency) dielectric constant of porous material. In what follows, the notation ε_w and ε_o designates the dielectric constant of the water and oil phases, respectively, whereas ε_S designates the dielectric constant of the solid phase. By invoking volume averaging, Revil (2013a) obtained

$$\varepsilon' = \frac{1}{F}[S_w^n \varepsilon_w + (1 - S_w^n)\varepsilon_o + (F-1)\varepsilon_S], \tag{21}$$

which can be simplified as

$$\varepsilon' = \frac{1}{F}[S_w^n \varepsilon_w + (1 - S_w^n)\varepsilon_o] + \varepsilon_S \tag{22}$$

for tight formations (recalling that $F \gg 1$). For anisotropic formations, equation 22 can be generalized as

$$\boldsymbol{\varepsilon} = \varepsilon_{ij} \mathbf{x}_i \otimes \mathbf{x}_j, \tag{23}$$

and

$$\varepsilon_{ij} = F_{ij}[S_w^n \varepsilon_w + (1 - S_w^n)\varepsilon_a] + \varepsilon^S_{ij}, \tag{24}$$

where ε^S_{ij} designates the components of the dielectric tensor of the solid phase $\boldsymbol{\varepsilon}_S = \varepsilon^S_{ij}{}''\mathbf{e}_i \otimes \mathbf{e}_j$. Note that the eigenvectors of this tensor correspond to the anisotropy of the solid matrix, and may be different from the eigenvectors associated with the tortuosity tensor of the pore space. In tight formations, the entries of $\boldsymbol{\varepsilon}_S$ can be obtained by taking the core sample in vacuo, and measuring the components of the dielectric tensor in different directions. That said, we expect that, in most conditions, the eigenvectors of the dielectric constant will be aligned with the eigenvectors of the complex conductivity tensor. Josh et al. (2012) observed that the anisotropy ratio can reach a factor of five for the high-frequency dielectric constant (>0.1 GHz).

Ampère's law in anisotropic media

The general form of Ampère's law in tight formations is, therefore, given by

$$\nabla \times \mathbf{H} = [\sigma_{\mathrm{eff}} - i\omega\varepsilon_{\mathrm{eff}}] \cdot \mathbf{E} \tag{25}$$

$$\boldsymbol{\varepsilon}_{\mathrm{eff}} = \varepsilon^{\mathrm{eff}}_{ij} \mathbf{x}_i \otimes \mathbf{x}_j, \tag{26}$$

$$\boldsymbol{\sigma}_{\mathrm{eff}} = \sigma^{\mathrm{eff}}_{ij} \mathbf{x}_i \otimes \mathbf{x}_j, \tag{27}$$

$$\sigma^{\mathrm{eff}}_{ij} \approx \sigma'_{ij} \approx F_{ij}(S_w^n \sigma_w) + T_{ij} s_w^p \rho_S \beta_{(+)}(1-f)\mathrm{CEC}, \tag{28}$$

and

$$\varepsilon^{\mathrm{eff}}_{ij} = F_{ij}[S_w^n \varepsilon_w + (1 - S_w^n)\varepsilon_a] + \varepsilon^S_{ij} - \frac{1}{\omega} T_{ij} S_w^p \rho_S \beta^S_{(+)} f_M \mathrm{CEC}. \tag{29}$$

The above equations neglect an important polarization mechanism in the intermediate frequency range (0.1 MHz–100 MHz), often referred to as Maxwell-Wagner polarization. This polarization mechanism is related to the discontinuity of displacement currents at interfaces of porous composites. According to Revil (2013a), Maxwell-Wagner polarization is nonnegligible, but not as important as often emphasized in the technical literature. We acknowledge that this mechanism should be included in future studies.

In the next section, we discuss the properties of the tortuosity and formation factor tensors and describe their definition for anisotropic porous material.

FORMATION FACTOR AND TORTUOSITY TENSORS

We first invoke the definition of two textural parameters, F and Λ, defined in previous studies (e.g., Johnson et al., 1986; Avellaneda and Torquato, 1991; Pride, 1994). The canonical boundary value problem for the normalized potential Γ of a cylindrical representative elementary volume of porous material of length L can be written as

$$\nabla^2 \Gamma = 0 \quad \text{in } V_{\mathrm{p}}, \tag{30}$$

$$\hat{\mathbf{n}}_s \cdot \nabla \Gamma = 0 \quad \text{on } S, \tag{31}$$

and

$$\Gamma = \begin{cases} L \text{ at} z = L \\ 0 \text{ at } z = 0 \end{cases} \quad \text{on } S, \tag{32}$$

where z denotes the distance along the axis of the cylindrical core. In the above equations, $\hat{\mathbf{n}}_s$ denotes the unit vector normal to the pore water/mineral interface, S (directed from the pore to the solid phase,

Figure 1), and V_p designates pore volume. Boundary conditions defining the normalized potential Γ are representative for the injection of an electrical current into a rock sample in the absence of surface conduction along the pore/water interface (see Johnson et al., 1986; Avellaneda and Torquato, 1991). The formation factor F is defined as (Johnson et al., 1986)

$$\frac{1}{F} = \frac{1}{V}\int_{V_p} |\nabla\Gamma|^2 \mathrm{d}V_p, \tag{33}$$

where V is the total volume of the considered representative elementary volume. Similarly, the tortuosity of the pore space is defined by Pride (1994) as

$$\frac{1}{\tau} = 1 + \frac{\hat{\mathbf{z}}}{V_p}\cdot\int_S \hat{\mathbf{n}}_s \Gamma \mathrm{d}S, \tag{34}$$

where the integration is performed over the surface of the grain/pore water interface S. Similarly, surface tortuosity could be defined from the surface formation factor introduced by Revil and Glover (1997). However, such surface tortuosity is required in our model for the reasons explained above.

In what follows, we designate $\mathbf{e} = -\nabla\Gamma$ the normalized electrical field (local electrical field divided by the norm of the macroscopic imposed field). The previous set of definitions can be readily generalized to the anisotropic case in the following manner:

$$\mathbf{F} = \frac{1}{V}\int_{V_p} \mathbf{e}\otimes\mathbf{e} dV_p, \tag{35}$$

and

$$T = \frac{1}{V_p}\int_{V_p} \mathbf{e}\otimes\mathbf{e}\mathrm{d}V_p. \tag{36}$$

Equations 35 and 36 show that $\mathbf{F}$ and $\mathbf{T}$ are symmetric.

Tortuosity and formation factor tensors can also be written in terms of three eigenvalues T^i (positive and less than one) for $\mathbf{T}$ and $(1/F_i)$ (F_i positive and greater than one) for $\mathbf{F}$ and the eigenvectors $\mathbf{t}^i$ as

$$\mathbf{T} = \sum_{i=1}^{3} T^i \mathbf{t}^i \otimes \mathbf{t}^i, \tag{37}$$

and

$$\mathbf{F} = \sum_{i=1}^{3} \left(\frac{1}{F^i}\right) \mathbf{t}^i \otimes \mathbf{t}^i. \tag{38}$$

For isotropic media, the above formulations simplify to the classical tortuosity and formation factor (see Bear [1988] for a description of the connectivity tensor),

$$T^1 = T^2 = T^3 = \frac{1}{\tau}, \tag{39}$$

and

$$F^1 = F^2 = F^3 = \frac{\tau}{\phi}. \tag{40}$$

The inverses of connectivity and conductivity formation factor tensors are obtained through the expressions

$$\mathbf{T}^{-1} = T_{ij}^{-1}\mathbf{e}_i \otimes \mathbf{e}_j = \sum_{i=1}^{3} \frac{1}{T^i}\mathbf{t}^i \otimes \mathbf{t}^i, \tag{41}$$

and

$$\mathbf{F}^{-1} = F_{ij}^{-1}\mathbf{e}_i \otimes \mathbf{e}_j = \sum_{i=1}^{3} F^i \mathbf{t}^i \otimes \mathbf{t}^i, \tag{42}$$

respectively. Note that for TI media, with (1, 2) being the symmetry plane, one has $F^1 = F^2 \neq F^3$ and $T^1 = T^2 \neq T^3$. The anisotropy ratio is defined as $\lambda = F^3/F^1 = T^3/T^1$. Mudrock formations are expected to have a petrofabric obeying this type of symmetry. In such a case, our model predicts that the anisotropy ratio for in-phase conductivity should be the same as that of quadrature conductivity. In addition, the anisotropy ratio for formation factor should be the same for surface and quadrature conductivites. We verify this prediction in the last section of the paper.

INFLUENCE OF ORGANIC MATTER AND KEROGEN CONTENT ON COMPLEX CONDUCTIVITY

As emphasized above, CEC plays a critical role in controlling not only the surface conductivity of clayey materials (Waxman and Smits, 1968), but also their quadrature conductivity (Vinegar and Waxman, 1984; Revil, 2012), or equivalently the low-frequency dielectric constant (Josh et al., 2012; Revil, 2013a). This behavior is illustrated in Figure 2 for the quadrature conductivity of porous siliciclastic materials.

In our model, quadrature conductivity can be expressed as a function of CEC as

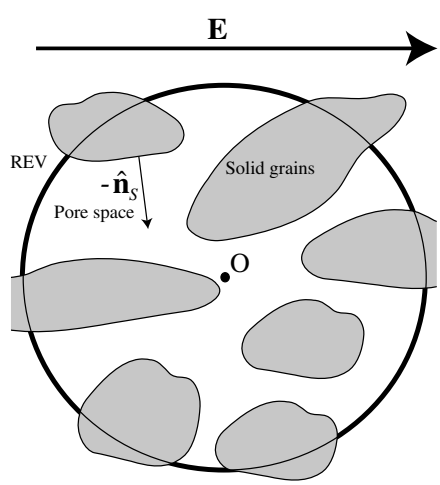

Figure 1. Description of the representative elementary volume (REV) centered at point O. Vector $\hat{\mathbf{n}}_s$ denotes the unit vector locally normal to the grains, $\mathbf{E}$ denotes the macroscopic electrical field applied to the REV. The local electric field is written as $\mathbf{e}$ in the main text and, in absence of electrical double layer, it is locally tangential to grain surfaces.

$$\boldsymbol{\sigma}'' = -\mathbf{b}\mathrm{CEC}_M, \tag{43}$$

and

$$\mathbf{b} = \beta^S_{(+)} f \rho_S \mathbf{T}. \tag{44}$$

For isotropic and kerogen-free materials, Figure 2 plots equation 43 with

$$\mathbf{b} = b\mathbf{I}, \tag{45}$$

($\mathbf{I}$ denotes the identity 3×3 matrix) and $b = 2.38 \times 10^{-7}$ S kg C^{-1} m^{-1} ($F\phi$ has been replaced by a tortuosity of 3/2, roughly the tortuosity of a path around spherical grains) against measurements. For fine-grained shales, tortuosity is expected to be much higher than 1.5. The last section of this paper shows that the tortuosity of bulk pore space of a mudrock can exceed 100. In turn, this behavior implies that for the same CEC, the quadrature conductivity of a mudrock is much smaller than for the case of a porous shaly sand (typically 1.5–3, see Vinegar and Waxman, 1984). Such an observation will also be discussed in the last section of the paper.

In Figure 3, we also test the proposition that, according to our model, the salinity dependence of quadrature conductivity is governed by the salinity dependence of the partition coefficient f. This salinity dependence is discussed in Appendix A. As f increases with salinity, we expect the magnitude of the quadrature conductivity to increase with salinity in agreement with what is shown in Figure 3 (see also Revil and Skold, 2011; Weller et al., 2011; Weller and Slater, 2012; Revil et al., 2013).

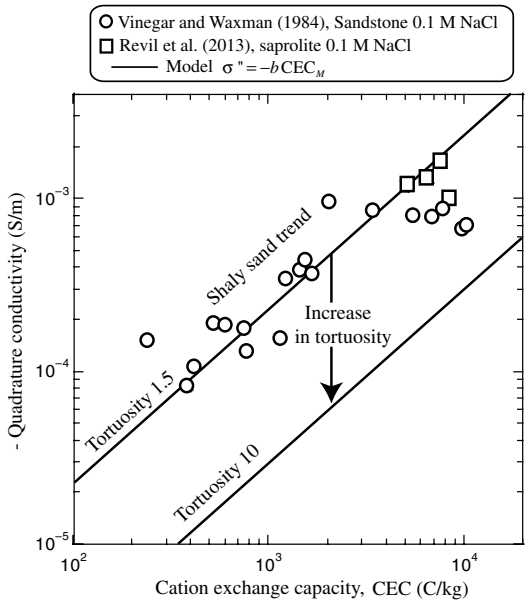

Figure 2. Linear relationship between quadrature conductivity and cation exchange capacity of clayey materials assuming fully saturated conditions (NaCl solution), equal salinity (0.1 M), same temperature, same frequency (approximately 10 Hz), and same pH range (5–7). The solid line was calculated for a tortuosity of 1.5. Higher tortuosities would generate lines parallel to the one shown but would predict smaller quadrature conductivity amplitudes for the same values of CEC and salinity.

In mudrocks (or in soils rich in organic matter), one may wonder about the role of kerogen or humic substances on complex conductivity. Kerogens are commonly present in high concentration in mudrocks, which clearly indicates they are potential source rocks for hydrocarbon deposits. However, this also indicates the solid phase comprises an additional component, which is characteristically distinct from the mineral rock matrix and should be accounted for in the analysis of complex conductivity.

To understand the CEC or specific surface area (SSA or S_{Sp}) of kerogen-rich rocks, it is important to emphasize the CEC or specific surface area of the kerogen itself. Few published works have considered the CEC/specific surface area measurements in oil or gas mudrocks. In that context, Derkowski and Bristow (2012) address the important question of whether sedimentary organic matter (mostly kerogen) in oil and gas mudrocks exhibits similar properties to those of organic matter found in soils. Indeed, during burial, organic matter has been subjected to pressure and temperature changes and these changes can alter the original properties.

Helling et al. (1964) report a CEC for organic matter in soils, for pH ranging from 6 to 8, in the range 1.6–2.1 meq g^{-1} [1 meq g^{-1} = 96, 320 C kg^{-1}, equating to $(1.5 - 2.0) \times 10^5$ C kg^{-1} in SI units]. Kaiser et al. (2007) report CEC values for organic matter of soils in the order of $(0.3 - 3.5) \times 10^5$ C kg^{-3} at pH 7. These values are extremely high and similar to the cation exchange capacity of smectite (about 1 meq g^{-1}, 10^5 C kg^{-3}, e.g., Revil, 2012), the clay mineral with the highest cation exchange capacity. Humus is known to have a CEC greater than smectite. This cation exchange capacity is explained by the high reactivity of the surface of organic matter as well as by the existence of isomorphic substitution in the organic macromolecules themselves (such as with smectite). Figure 4 shows different reactive sites on the surface of organic

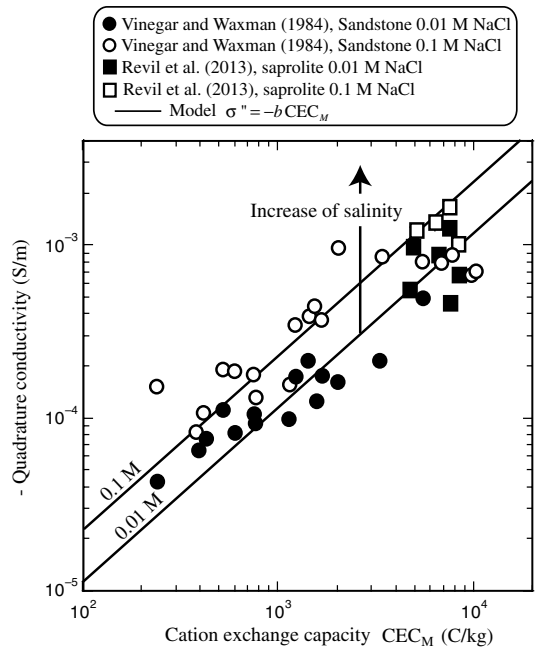

Figure 3. Influence of the salinity on the magnitude of quadrature conductivity. The increase of salinity is responsible for an increase of the magnitude of quadrature conductivity. In our model, this effect is related to the effect of salinity on the partition coefficient f of counterions in the Stern layer.

matter that are responsible for their high CEC. At nearly neutral pH values, the number of electrical charges per unit surface area can be determined as the ratio of total charge per unit mass CEC to total surface area per unit mass SSA; for humus: 559 cMol kg^{-1} (5.6×10^5 C kg^{-3}) by 7.2×10^5 m^2 kg^{-1}; this yields a surface charge of 0.78 C m^{-2} (about five elementary charge per nm^2), a value that is approximately twice that of clays (e.g., Woodruff and Revil, 2011).

The CEC and specific surface area of soil or oil mudrocks can therefore be written as

$$\mathrm{CEC} = \sum_{i=1}^{N} \chi_i \mathrm{CEC}_i, \tag{46}$$

and

$$\mathrm{S}_{sp} = \sum_{i=1}^{N} \chi_i \mathrm{S}_{sp,i}, \tag{47}$$

where N is the number of the mineral phases (including kerogen in oil mudrocks or organic matter in soils) and χ_i denotes the mass fraction of the ith mineral with respect to the total mass of dry solid. In oil mudrocks, CEC can be expected to be dominated by clay minerals and kerogen, whereby

$$\mathrm{CEC} = \chi_\mathrm{K}\mathrm{CEC}_\mathrm{K} + \chi_\mathrm{I}\mathrm{CEC}_\mathrm{I} + \chi_\mathrm{S}\mathrm{CEC}_\mathrm{S} + \chi_\mathrm{Ke}\mathrm{CEC}_\mathrm{Ke}, \tag{48}$$

and

$$\mathrm{S}_{sp} = \chi_\mathrm{K}\mathrm{S}_{sp,\mathrm{K}} + \chi_\mathrm{I}\mathrm{S}_{sp,\mathrm{I}} + \chi_\mathrm{S}\mathrm{S}_{sp,\mathrm{S}} + \chi_\mathrm{Ke}\mathrm{S}_{sp,\mathrm{Ke}}, \tag{49}$$

where the subscripts K, I, and S refer to kaolinite, illite, and smectite, respectively, and Ke refers to kerogen. There are five types of kerogen defined in the literature: type I (sapropelic, formed from protein and lipids of mostly algae), type II (planktonic, formed from lipids of plankton deposited under reducing conditions), type II-S (similar to type II with a high sulfur content), type III (humic, from terrestrial plants), and type IV (contains mostly decomposed organic matter). It is possible that the CEC and SSA of kerogen may depend on the type and maturity of kerogen as well.

The CEC of humic matter and kerogen can be related to the quantity of carbon in oil mudrocks. For soils that are rich in organic matter, it is known that cation exchange capacity is highly correlated with carbon content (Figure 5). Therefore, one could expect a correlation between TOC (total amount of organic carbon content in weight%) of kerogen and cation exchange capacity of the material. That said, experimental results available in the literature are conflicting (see the discussion in Derkowski and Bristow, 2012). The CEC of kerogen is believed to be very small compared to the CEC of organic matter in soils because all the available exchangeable sites in functional groups shown in Figure 4 may have been polymerized during burial (see Vandenbroucke and Largeau, 2007). Derkowski and Bristow (2012) indicate that the thermal treatment used prior to CEC measurements can reactivate some of these functional sites (possibly through the deprotonation of carboxylic acids) and lead to a CEC associated with kerogen that may explain conflicting results found in the literature. Derkowski and Bristow (2012) observed an inverse relationship between kerogen maturity and the amount of carboxylic groups. It then follows that immature kerogen has greater susceptibility to thermal activation. Therefore, the thermal treatment applied to less mature kerogen may substantially increase the CEC of the material, as well as surface conduction and quadrature conductivity (polarization).

In summary, we believe that the CEC of kerogen can be neglected in the evaluation of the quadrature conductivity of hydrocarbon-bearing tight mudrocks (Derkowski and Bristow, 2012) but not the specific surface area, which can be very high. Derkowski and Bristow (2012) report a specific surface area in the range from 700 to 920 m^2 g^{-1} for kerogen extracted from the mature Red Bird and Monterey formations. This represents a range of values very similar to that measured for smectite (e.g., Woodruff and Revil, 2011). For the Woodford formation, Derkowski and Bristow (2012) measure the excess specific surface area not accounted for by clay minerals. As shown in Figure 6, such an excess surface area is correlated with total amount of organic carbon content (in weight %). The relationship can be written as

$$\mathrm{S}_{sp}(\mathrm{Kerogen}) = a\,\mathrm{TOC}(\%), \tag{50}$$

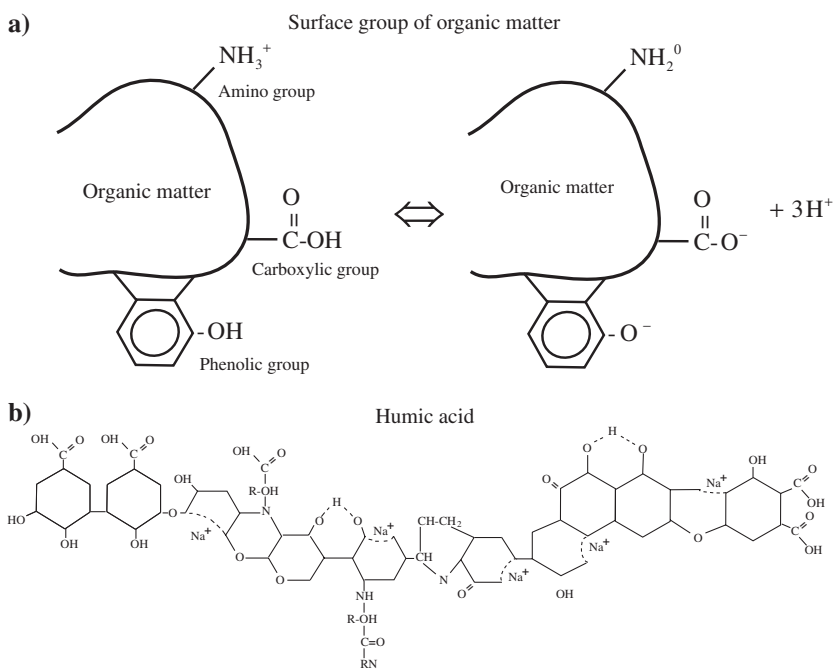

Figure 4. Surface sites of organic substances such as humic acids. (a) The surface of organic matter is generally negative at neutral pH values and is characterized by very high values of specific surface area and cation exchange capacity. Surface charge can be positive below pH 2. In addition to a pH-dependent charge on the surface of these macromolecules, there is a permanent electric charge associated with isomorphic substitutions. (b) Example of humic acid (Leonardite) showing different types of surface sites. Note that CEC also increases with oxidation of such organic molecules.

where $a \approx 10$. For pure kerogen, the above expression yields [TOC(%) = 100] a specific surface area of 1000 $m^2\,g^{-1}$, which is only slightly higher than values given above. Therefore, specific surface area is given by

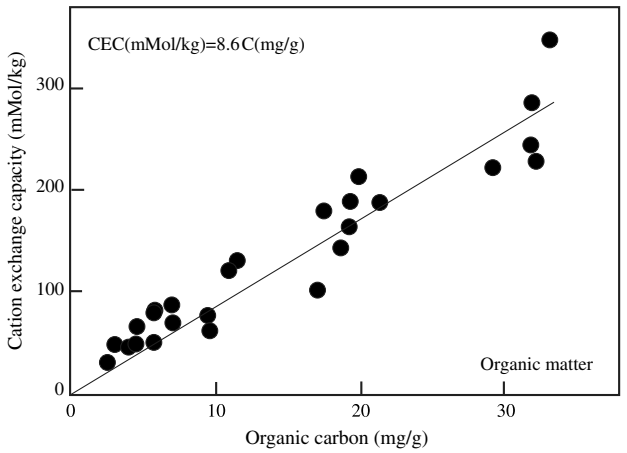

Figure 5. Correlation between cation exchange capacity (CEC) of organic matter and amount of organic carbon (weight concentration, experimental data from Liang et al., 2006).

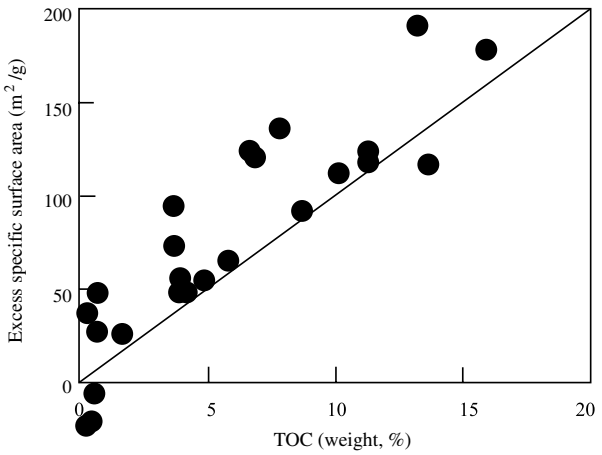

Figure 6. Relationship between excess specific surface area (clay contribution removed) and total organic content (weight %) for kerogen-rich oil shales. Data from Derkowski and Bristow (2012) for the Woodford formation.

$$S_{sp} = \chi_{\mathrm{Clay}} S_{sp,\mathrm{clay}} + S_{sp,\mathrm{Ke}} \mathrm{TOC}, \tag{51}$$

where TOC is expressed in mass fraction (in %). However, it is unclear at this point whether kerogen would impact the quadrature conductivity through its surface area. In principle, if there is no Stern layer associated with kerogen (no reactive sites), presence of kerogen in oil and gas mudrocks should have no impact on quadrature conductivity. Therefore if the specific surface area is used to assess the quadrature conductivity, the former should be corrected for the contribution of kerogen. The TOC content might also change the tortuosity of the porous body and indirectly affect the bulk conductivity. Furthermore, if bitumen is present, the polar components might contribute to the surface conductivity. However, these effects need to be verified by experimental evidence.

COMPARISON TO EXPERIMENTAL DATA

Material and methods

This section analyzes the complex conductivity of two Bakken core samples. The Bakken formation is a Late Devonian Early Mississippian shale (deposited approximately 360 millions of years ago) located in the Williston Basin, underlying parts of Montana, North Dakota, and Saskatchewan. sample A was acquired at a depth of 2630 m whereas sample B was acquired at 3098 m. The deeper sample, sample B, is from the higher-temperature, central portion of the Williston Basin, whereas the second core sample is from the basin's margin. Table 1 summarizes the properties of the two core samples. Porosity was measured by hydrogen adsorption, which does not account for the percentage weight (wt%) of kerogen; 20 wt% kerogen results in 40–70 vol% kerogen, depending on the density of the kerogen (Prasad et al., 2011). Average nonkerogen porosity in Bakken shale samples is approximately 3%.

Spectral induced-polarization measurements were performed using an apparatus developed at the Central Laboratory for Electronics, ZEL, at the Forschungszentrum Jülich, in Germany by Zimmermann et al. (2008). Various tests of this impedance meter are documented by Revil and Skold (2011) and will not be repeated here. Electrodes used were sintered Ag/AgCl, 2 mm pellet electrodes for voltage measurements, and transcutaneous electrical nerve stimulation (TENS) adhesive electrodes for current injection (see Figure 7 for a description of the position of the electrodes).

The Bakken samples were saturated with three pore-water solutions of varied salinity derived from an equilibrium solution obtained by saturating (distilled) DI water with a soluble mineral fraction of pulverized core fragments. A low-salinity limit of 0.5 mM was estimated as the equilibrium concentration of NaCl. Solutions were also prepared for 0.05 and 0.5 M. The samples were initially saturated with equilibrium water under sequential

Table 1. Properties of the two core samples. Porosity is nonkerogen matrix porosity measured with a He pycnometer. The reported density is bulk density (grain density is estimated at 2650 $kg\,m^{-3}$). Reference depth: Kelly bushing.

Sample	Depth (m)	ϕ	Density ($kg\,m^{-3}$)	TOC (wt%)	Hydrogen index	Maturation
Bakken A	2630	0.028	1990	20.1	584	II
Bakken B	3098	0.032	2220	12.1	436	III

pressurizations up to 10.3 MPa (1500 psi), and resaturated with the remaining solutions in two stages. Spectral-induced-polarization acquisitions were made at each of the three stages. Due to the low diffusion coefficient for the NaCl solution in the samples, approximately 10^{-11} m^2 s^{-1} (Revil et al., 2005), the equilibration time at each stage is in the order of several weeks (the average radius of the cylindrical samples is 0.010 m, yielding $1 \times 10^{-4}/2.5 \times 10^{-11} = 4 \times 10^6$ s $\approx$ 46 days). The brine is degassed prior to the saturation. The saturated samples are immersed in the respective equilibrium solution and stored at low pressure close to vacuum conditions.

Complex spectra of the eigenvalues of the electrical impedance tensor were obtained directly by following the single-component polarization protocol with the four-electrode impedance spectroscopy method developed by Zimmermann et al. (2008). The Bakken B specimens are cylindrical cores with a radius of 12.6 mm and heights of 38.3 and 30.8 mm for the in-plane (longitudinal) and transverse directions, respectively; geometric factors were obtained numerically using a Comsol Multiphysics simulator. We perform the measurements at laboratory temperature and pressure; we

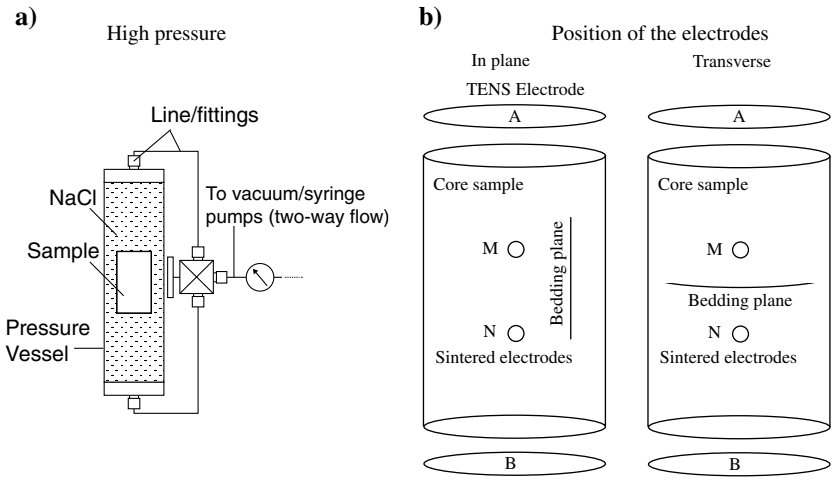

Figure 7. Cell and geometry of measurement acquisition for transverse and in-plane electrical conductivity measurements with respect to bedding plane. (a) Sketch of the cell. (b) Geometry of the electrodes. A and B denote current electrodes whereas M and N denote voltage electrodes. The geometric factor was computed as $k = A/L$, where L is the distance between the M and N electrodes (1/3 of the height of the sample) and A is the cross-sectional area of the cylindrical core sample. The current electrodes are coupled to the sample with a conductive electrolytic gel-adhesive (designed for use on human skin in nerve stimulation therapy applications), whereas the potential electrodes are coupled to the sample through a conductive electrolyte gel. The current electrodes can be removed and reused in repeat acquisitions; here depicted as detached from the sample to illustrate the size and shape, corresponding to the end-faces of the sample. The sample surface (except at the position of the electrodes) is covered with quick dry nail polish, which prevents desaturation and is a good insulator.

Table 2. In-phase σ' and quadrature σ'' conductivities at different salinities (I stands for in-plane measurements whereas T stands for transverse measurements with respect to bedding plane).

	0.5 mM		0.05 M		0.5 M	
	In-phase	Quadrature	In-phase	Quadrature	In-phase	Quadrature
Bakken A-I	$7.82E-03$	$2.91E-05$	$1.01E-02$	$3.46E-05$	$1.54E-02$	$6.59E-05$
Bakken A T	$8.87E-04$	$4.65E-06$	$1.17E-03$	$5.52E-06$	$1.96E-03$	$4.03E-06$
Bakken B-I	$3.33E-04$	$6.29E-06$	$1.53E-03$	$2.06E-05$	$3.15E-03$	$3.21E-05$
Bakken A-T	$4.73E-05$	$9.23E-07$	$1.53E-04$	$2.72E-06$	$9.22E-04$	$4.05E-06$

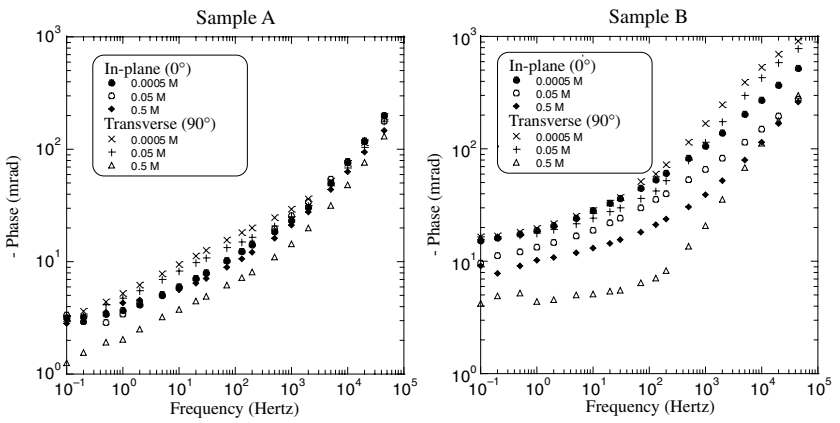

Figure 8. Measured phases for samples A and B. Note the continuous increase of the magnitude of the phase with the frequency. The high-frequency response is likely due to Maxwell-Wagner polarization.

coated the samples in quick dry nail polish to prevent evaporation at the core surface, as well as impose an insulating boundary, constituting a closed electrical system for the measurements. With this approach, no sample holder is required. The coating is easily removed with acetone to maximize surface exposure for subsequent pressurizations. Spectral complex conductivity tensors were determined from the measured directional impedances of the samples. Table 2 summarizes the in-phase and quadrature conductivity of the two core samples at 1 Hz.

We also performed spectral induced polarization at five different stages, referred to below as stages I through V, during the pressurized saturation sequence, capturing unsaturated measurements at different water contents for sample B. The samples were pressurized at increasing sequential maximum confining (hydrostatic) pressures of 0.69, 3.45, 6.89, and 10.34 MPa. Stages I and II were completed in two successive 24 hour periods, and stages III and IV in successive 48 hour periods. An additional measurement was made after 30 days to represent the final saturation state, stage V (the datasets of stages IV and V are equivalent, evidencing full saturation of the sample; the stage V measurements are used in our analysis). The water content is determined through gravimetric monitoring at each saturation stage.

Results under saturated conditions

Figure 8 shows the raw data for the phase. The tangent of the phase angle is defined as the ratio of quadrature conductivity to in-phase conductivity. Figure 8 reveals only a fair agreement between the phases measured in the in-plane and transverse directions of the core samples at low frequencies. The magnitude of the phase increases slightly with frequency below 100 Hz and faster above 100 Hz. The polarization of the electrical double layer is expected to dominate the response of the quadrature conductivity below 100 Hz, whereas above 100 Hz, the response is partly controlled by the true dielectric polarization of the material with some influence from the Maxwell-Wagner polarization (see Revil, 2013a) and possibly some electromagnetic coupling effects.

The complex conductivity spectra are plotted as a function of frequency for the three salinities in Figure 9 for sample A, and in Figure 10 for sample B. In-phase conductivity data display only weak dependence with respect to frequency as already observed for other clay-rich materials (see Vinegar and Waxman, 1984; Slater and Lesmes, 2002; Revil, 2012). Quadrature conductivity spectra exhibit a plateau at low frequencies and an increase in magnitude at high frequencies due to Maxwell-Wagner polarization and true dielectric polarization (Revil, 2013a).

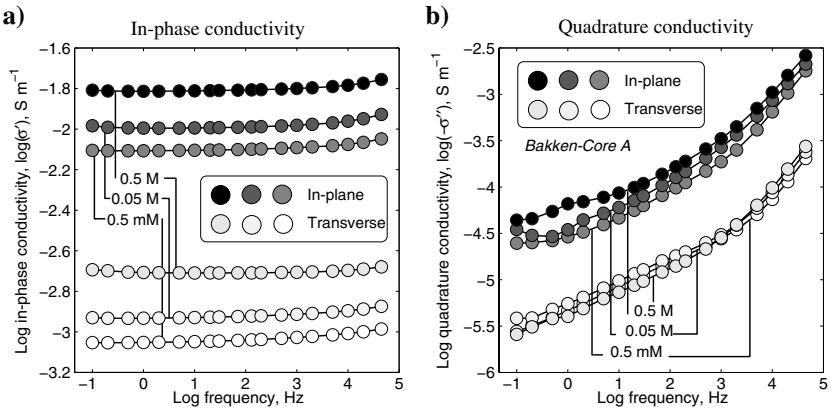

Figure 9. Complex conductivity spectra for Bakken core sample A. (a) In-phase electrical conductivity versus frequency at three salinities (0.5, 0.05, and 0.005 M NaCl). (b) Quadrature electrical conductivity versus frequency at three salinities (0.5, 0.05, and 0.005 M NaCl).

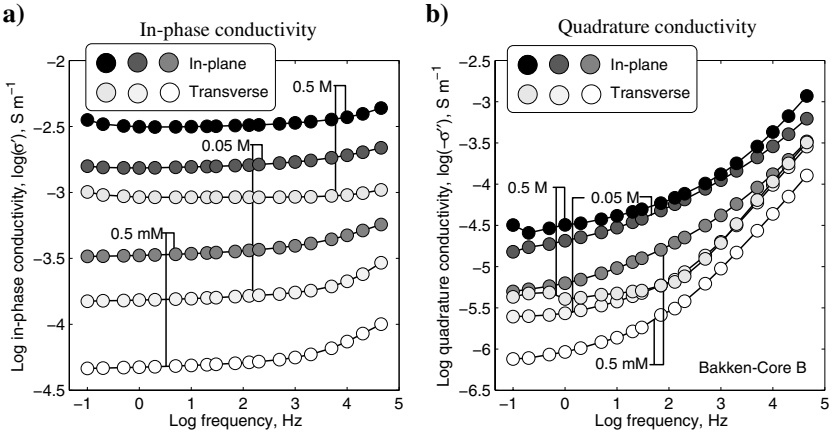

Figure 10. Complex electrical conductivity spectra of Bakken core sample B. (a) In-phase electrical conductivity versus frequency at three salinities (0.5, 0.05, and 0.005 M NaCl). (b) Quadrature electrical conductivity versus frequency at three salinities (0.5, 0.05, and 0.005 M NaCl).

We first test our prediction regarding anisotropy ratio for in-phase and quadrature conductivities (see Figure 11). The mean anisotropy ratio is 8.1 ± 3.1 ($N = 12$, N: number of measurements) for in-phase and quadrature conductivity data acquired together for the two core samples (7.6 ± 2.3, $N = 6$, for the in-phase conductivity and 8.5 ± 3.8, $N = 4$, for the quadrature conductivity). The anisotropy ratio is approximately the same for in-phase and quadrature conductivities. This behavior is consistent with the predictions of our model.

We now focus on the relationship between in-phase conductivity and pore water conductivity of NaCl solutions. Electrical conductivity of water can be described using the semiempirical relation derived by Sen and Goode (1992), i.e.,

$$\sigma_f(C_f;T) = (d_1 + d_2T + d_3T^2)C_f - \frac{d_4 + d_5T}{1 + d_6C_f}(C_f)^{3/2}, \tag{52}$$

where $d_1 = 5.6$, $d_2 = 0.27$, $d_3 = -1.51 \times 10^{-4}$, $d_4 = 2.36$, $d_5 = 0.099$, $d_6 = 0.214$, σ_f is electrical conductivity of water (in $\mathrm{S\,m^{-1}}$), T is temperature (in °C) and C_f is salinity (in M, mol L^{-1}). This relation yields pore water conductivities of $3.82\ \mathrm{S\,m^{-1}}$, $0.49\ \mathrm{S\,m^{-1}}$, and $0.0054\ \mathrm{S\,m^{-1}}$. Figure 11 shows the corresponding in-phase and quadrature conductivities as a function of conductivity of pore-water solution. The relationship between in-phase conductivity and pore-water conductivity is used to determine formation factor and surface conductivity in the in-plane and transverse directions with respect to bedding plane. Table 3 reports the formation factors and surface conductivities, together with the determination of Archie's porosity exponent ($m = -\ln F/\ln \phi$ in the two directions) and tortuosity ($\tau = F\phi$). For samples A and B, the surface conductivity anisotropy ratios are 8.8 ± 0.9 and 7.4 ± 0.8, respectively. These values are comparable to the anisotropy ratios for the quadrature conductivity, 6.3 ± 0.7 and 6.8 ± 0.8, respectively for samples A and B.

The immature sample A may have higher clay content, which could explain the higher surface conductivity than observed for sample B. Regarding quadrature conductivity, the in-plane (I) and transverse (T) quadrature conductivities are given by

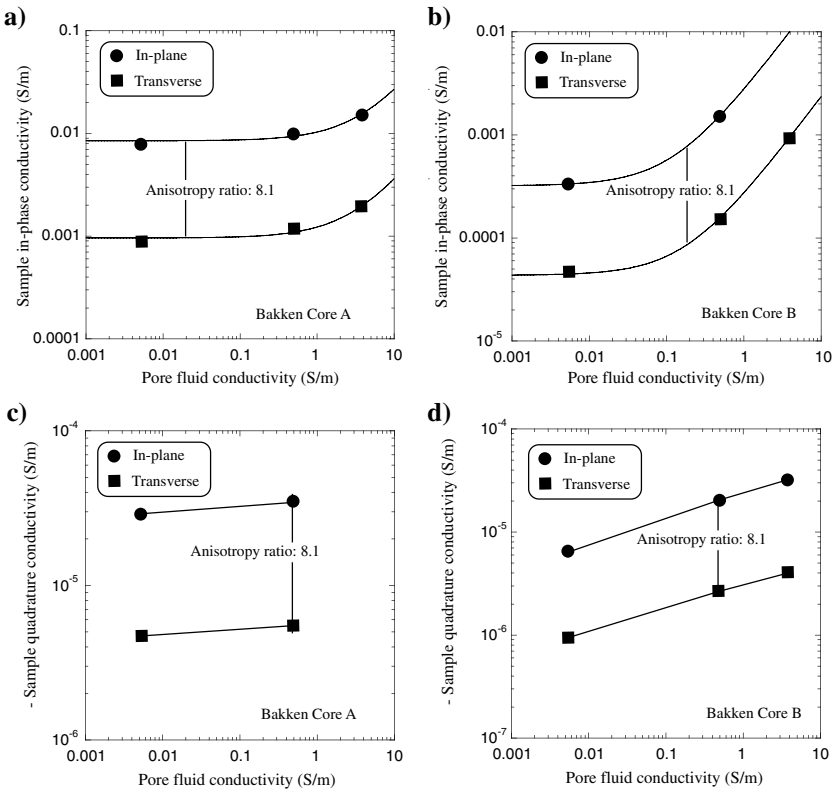

Figure 11. In-phase and quadrature electrical conductivities for core samples A and B at 1 Hz. (a) In-phase electrical conductivity, sample A. Lines identify the model fit (equation 5 at saturation). (b) In-phase conductivity, sample B. For the two upper graphs, the lines identify the model fit. Formation factors and surface conductivities are reported in Table 3. (c) Quadrature electrical conductivity, sample A (the points at the highest salinity are not shown because of their uncertainties). The vertical line serves as guide. (d) Quadrature conductivity, sample B. For the two lower graphs, the lines serve as guides. Anisotropy ratio is defined as the ratio of the highest to the lowest eigenvalues of the tensor; it exhibits a mean of 8.1 ± 3.1 ($N = 12$).

Table 3. Formation factor F, surface conductivity σ_S, porosity exponent m, and tortuosity τ (I stands for in-plane measurements and T stands for transverse measurements with respect to bedding plane). The tortuosity in a given direction is determined by the product of the formation factor times porosity.

Sample	F(I)	F(T)	σ_S (I, $\times 10^{-4}$ S/m)	σ_S (T, $\times 10^{-4}$ S/m)	m(I)	m(T)	τ(I)	τ(T)
Bakken A	543 ± 100	3770 ± 530	84 ± 7	9.6 ± 0.8	1.76	2.30	15.2	106
Bakken B	406 ± 130	4350 ± 30	3.2 ± 0.8	0.43 ± 0.03	1.75	2.43	13.0	139

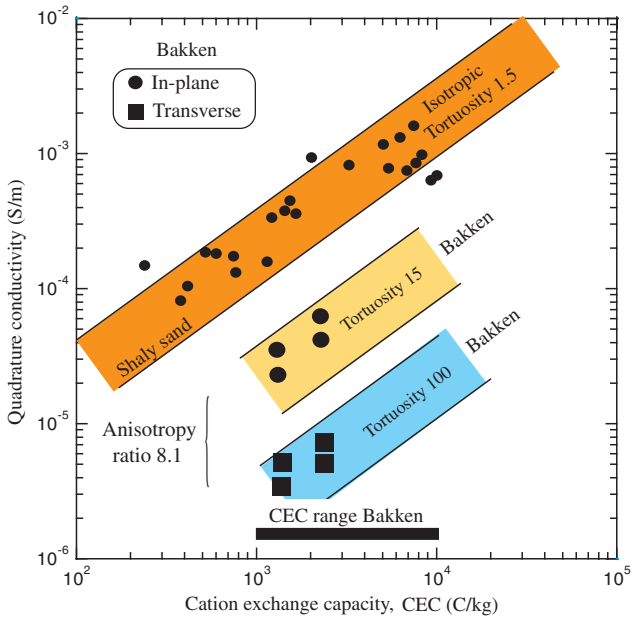

Figure 12. Influence of anisotropy and tortuosity upon quadrature conductivity (1 Hz). The high tortuosities found in Bakken rocks are responsible for a decrease of quadrature conductivity at a given salinity and CEC. For Bakken rock samples, data are consistent with a tortuosity value of 15 in the bedding plane and over 100 in the transverse direction.

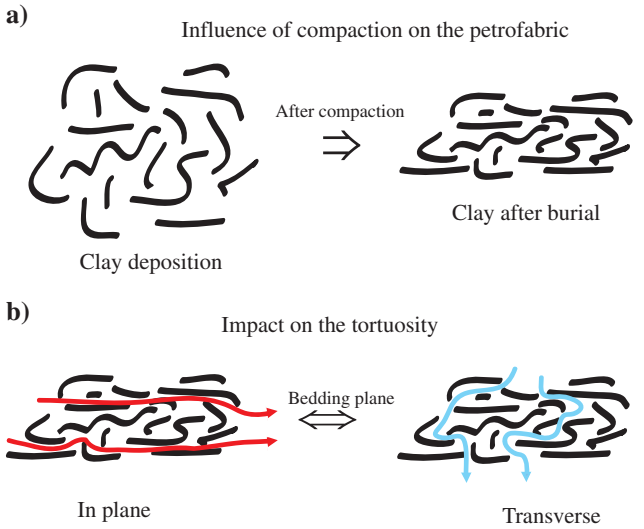

Figure 13. Influence of burial on petrofabric and tortuosity tensor. (a) Differential compaction is responsible for the formation of petrofabric in clayey materials (clay particles are shown in black). Depositional facies and burial are typically responsible for the formation of TI (transversely isotropic) media. (b) In TI media, the in-plane tortuosity is expected to be much smaller than the tortuosity in the direction transverse to bedding plane.

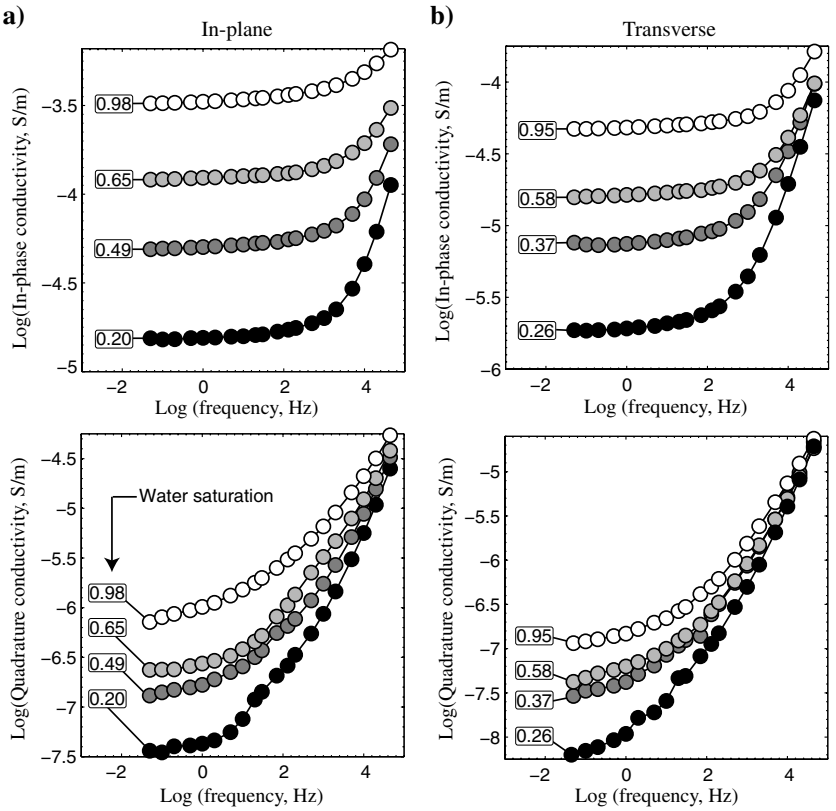

Figure 14. Influence of saturation upon in phase and quadrature conductivities of sample B. (a) In-plane measurements for in-phase and quadrature conductivities. (b) Transverse measurements for in-phase and quadrature conductivities. Note that a change in saturation affects the magnitude of the in-phase and quadrature conductivities, not the anisotropy ratio. This result is consistent with our assumption to consider that n and p do not depend too much on the direction.

$$\sigma''(I) = -\frac{\beta^S_{(+)} f \rho_S}{\tau_I} \mathrm{CEC}_M, \tag{53}$$

and

$$\sigma''(\mathrm{T}) = -\frac{\beta^S_{(+)} f \rho_S}{\tau_T} \mathrm{CEC}_M, \tag{54}$$

whereas surface conductivities in the in-plane and transverse directions are given by

$$\sigma_S(I) = \frac{\rho_S \beta_{(+)}(1-f)}{\tau_I} \mathrm{CEC}_M, \tag{55}$$

and

$$\sigma_S(T) = \frac{\rho_S \beta_{(+)}(1-f)}{\tau_T} \mathrm{CEC}_M, \tag{56}$$

respectively, where $\beta_{(+)}(\mathrm{Na}^+, 25°\mathrm{C}) = 5.2 \times 10^{-8}\ \mathrm{m^2\,s^{-1}\,V^{-1}}$ and $\beta^S_{(+)}(25°\mathrm{C}, \mathrm{Na}^+) = 1.5 \times 10^{-10}\ \mathrm{m^2\,s^{-1}\,V^{-1}}$ for clay minerals (Revil, 2012, 2013a, 2013b). We first determine the CEC using equations 53 and 54, and f close to one. Very consistent values are obtained at high salinities with $\mathrm{CEC} = 2500 \pm 300\ \mathrm{C\,kg^{-1}}$ for sample A and $\mathrm{CEC} = 1200 \pm 300\ \mathrm{C\,kg^{-1}}$ for sample B. This behavior agrees with the known CEC of the Bakken shale, which is in the order of 10^{-2} to 10^{-1} $\mathrm{meq\,g^{-1}}$ (about 1000 to 10,000 $\mathrm{C\,kg^{-1}}$; data obtained from the North Dakota Industrial Commission, Department of Mineral Resources, Oil and Gas Division online subscription database. Using equations 55 and 56, we obtain $f = 0.78 \pm 0.03$ for sample A and $f = 0.99$ for sample B. The values of CEC and f obtained by our model are consistent with the expected their respective relationship to clay type, and may imply that sample A is richer in smectite and that sample B is rich in kaolinite.

Figure 12 describes the impact of anisotropy and increase of tortuosity for the Bakken shale by comparison to shaly sands investigated by Vinegar and Waxman (1984) and the saprolites investigated by Revil et al. (2013). As predicted by our model, at given values of CEC and salinity, the magnitude of quadrature conductivity is expected to decrease with the increase of tortuosity and differ in the in-plane and transverse directions (respective to bedding. Tortuosity in the in-plane direction is also found to be much smaller than in the transverse direction. As shown in Figure 13a, differential compaction during burial is responsible for the formation of a bedding plane with the shale, thereby becoming a TI medium. In this case, we expect the tortuosity in the in-plane direction to be substantially smaller than in the transverse direction (Figure 13b). Tortuosity in this case can also be related to the aspect ratio of grains, as discussed in Mandelson and Cohen (1982). Other published experimental works have report very high tortuosities; for instance Revil et al. (1996) reported tortuosities in the range of 2–46 for doleritic core samples. Zhang and Scherer (2012, their Table 6) have report electrical tortuosities in the range 2–118 for tight shales. Values higher than 100 were obtained for very tight specimens with porosities below 3%.

Results under unsaturated conditions

Figure 14 shows the in-phase and quadrature conductivities of sample B at different saturations. It is clear from this figure that saturation does not change the anisotropy ratio of the material. In-phase and quadrature conductivity data are plotted as a function of saturation in Figure 15. Measurements are fitted with a power-law relationship to determine the saturation n-exponent and the p-exponent describing the saturation dependence of quadrature conductivity. The first observation is that the n and p exponents do not exhibit significant anisotropy ($n = 2.7 \pm 0.4$ in the in-plane direction and $n = 2.4 \pm 0.3$ in the transverse direction, and $p = 1.8 \pm 0.1$ in the in-plane direction and $p = 1.4 \pm 0.2$ in the transverse direction). Figure 16 reports the values of the two exponents together with the n and p exponents of isotropic sedimentary materials (see Revil, 2013a). All the data conform fairly well to the general trend $p = n - 1$.

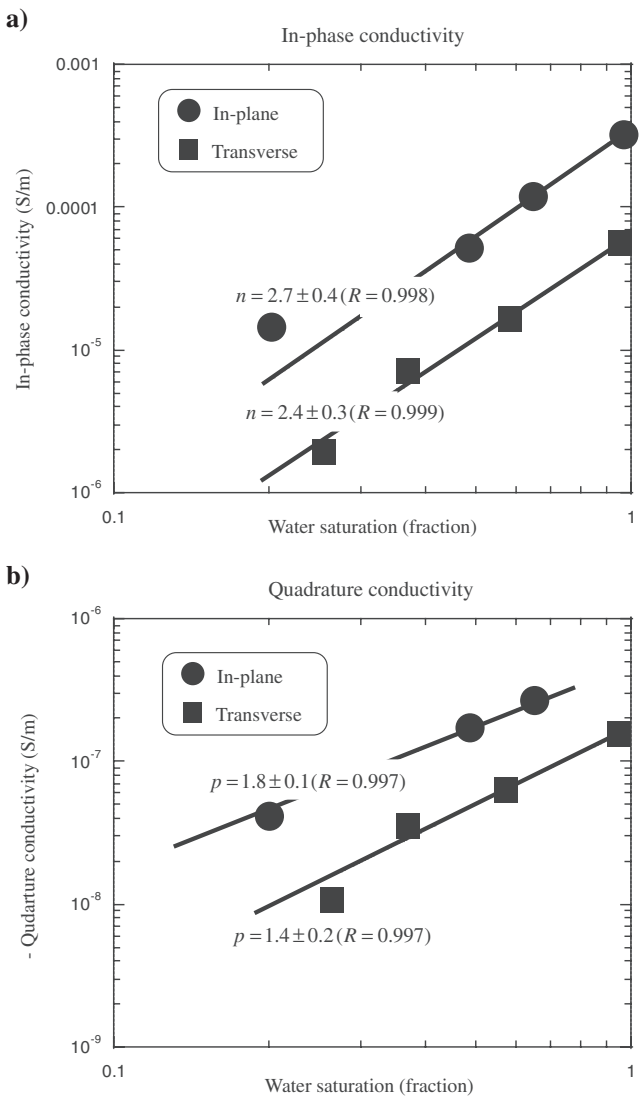

Figure 15. Influence of the saturation on the in-phase and quadrature conductivity of sample B at 1 Hz. (a) In-phase conductivities (in-plane and transverse measurements). (b) Quadrature conductivities (in-plane and transverse measurements).

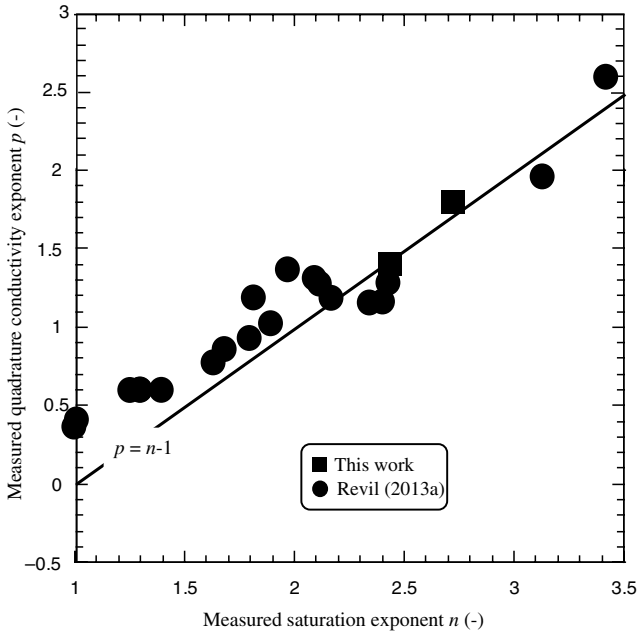

Figure 16. Relationship between the p-exponent used to describe the saturation dependence of the quadrature conductivity and the n-exponent (saturation exponent) used to describe the saturation dependence of the in-phase conductivity when surface conductivity is negligible. The plain line corresponds to the relationship developed in Revil (2013a), which is consistent with the prediction of the model of Vinegar and Waxman (1984).

CONCLUSIONS

We introduced a new petrophysical model to describe the complex electrical conductivity tensor of oil mud-rocks. The model accounts for anisotropy, saturation, porosity, and cation exchange capacity/specific surface area of rocks. Verification experiments were performed on two core samples from the Bakken formation. The following conclusions stem from the work presented in this paper:

1) In-phase electrical conductivity is controlled by a formation factor tensor whereas quadrature conductivity is controlled by a tortuosity tensor of the bulk pore space. Both tensors are interrelated through the connected porosity.
2) The CEC of kerogen is believed to be very small in comparison to the CEC of organic matter in soils. Indeed, because of diagenesis, all the exchangeable sites in the functional groups of organic matter may have been polymerized; therefore, the surface of kerogen may not impact surface and quadrature conductivity of oil and gas mud-rocks.
3) Experimental data confirmed our model prediction that the anisotropy ratio is the same for in-phase and quadrature conductivities. It was also confirmed that the anisotropy ratio is the same for formation factor and surface conductivity. The anisotropy ratio for the complex conductivity tensor is 8.1 ± 3.1 for the two Bakken core samples. Our model predicts an invariant phase angle for in-plane (I) and transverse (T) measurements for all frequencies. This behavior is only approximately shown by the experimental data acquired at low frequencies; additional data will be needed for verification.
4) Measurements performed on two rock samples from the Bakken formation indicate that our model provides a simple explanation for (a) the dependence of quadrature conductivity on salinity and (b) the effect of increase of tortuosity on the decrease of the magnitude of quadrature conductivity. The bulk tortuosity in the direction transverse to the bedding plane is found to be higher than 100. This very high value of tortuosity is likely associated with the aspect ratio of grains.
5) The decrease of saturation does not significantly change the degree of anisotropy observed for the quadrature and in-phase conductivities under saturated conditions. It follows that the p-exponent characterizing the saturation dependence of quadrature conductivity can be related to the saturation exponent n by $p = n - 1$.

ACKNOWLEDGMENTS

This work was funded by The University of Texas at Austin's Research Consortium on Formation Evaluation, jointly sponsored by Anadarko, Apache, Aramco, Baker-Hughes, BG, BHP Billiton, BP, Chevron, China Oilfield Services, LTD., ConocoPhillips, ENI, ExxonMobil, Halliburton, Hess, Maersk, Marathon Oil Corporation, Mexican Institute for Petroleum, Nexen, ONGC, Petrobras, Repsol, RWE, Schlumberger, Shell, Statoil, Total, and Weatherford. We also than the Oclassh research project and its sponsor (Chevron, Repsol, Whiting, Venoco, Shell, Aramco, Magrtek, and Hess). We thank Egon Zimmermann for the construction of the impedance meter, Andreas Weller and an anonymous referee for their constructive reviews of our manuscript, and the associate editor for the speed of the review process.

APPENDIX A

We introduce a simple model to describe the dependence of salinity on the partition coefficient f. Consider first the sorption of sodium in the Stern layer of clays and the dissociation of protons according to the following, simplified speciation model

$$> SH^0 \Leftrightarrow > S^- + H^+, \tag{A-1}$$

and

$$> S^- + Na^+ \Leftrightarrow > S^-Na^+, \tag{A-2}$$

where $>$S designates the surface (amphoteric) sites attached to the crystalline framework, H^0 are protons (which are assumed to be immobile), whereas weakly sorbed Na^+ (which are known to keep their hydration layer) are assumed mobile in the Stern layer. Equilibrium constants for the reactions A-1 and A-2 are given by

$$K_{Na} = \frac{\Gamma^0_{SNa}}{\Gamma^0_{S^-}[Na^+]^0}, \tag{A-3}$$

and

$$K_H = \frac{\Gamma^0_{S^-}[H^+]^0}{\Gamma^0_{SH}}. \tag{A-4}$$

The conservation equation for the surface species is given by

$$\Gamma^0_{\mathrm{S}} = \Gamma^0_{\mathrm{SNa}} + \Gamma^0_{\mathrm{SH}} + \Gamma^0_{\mathrm{S^-}} + \Gamma^0_{\mathrm{X}}, \tag{A-5}$$

where Γ^0_{S} denotes the total surface site density (including charge associated with isomorphic substitutions in the crystalline framework), Γ^0_{SNa}, $\Gamma^0_{\mathrm{S^-}}$, and Γ^0_{SH} designate the surface charge density of the sites $>\mathrm{S^-Na^+}$, $>\mathrm{S^-}$, and $>\mathrm{SH^0}$, respectively, and Γ^0_{X} represents the number of equivalent sites corresponding to isomorphic substitutions (all expressed in sites $\mathrm{m^{-2}}$). To simplify notation, we write $\mathrm{pH} = -\log_{10}[\mathrm{H^+}]$, whereas $[\mathrm{Na^+}] = C_f$ denotes the salinity of the pore water solution. The resolution of equations A-3, A-4, and A-5 yields

$$\Gamma^0_{\mathrm{SH}} = \frac{\Gamma^0_{\mathrm{S}} - \Gamma^0_{\mathrm{X}}}{1 + \frac{K_{\mathrm{H}}}{10^{-\mathrm{pH}}}(1 + C_f K_{\mathrm{Na}})}, \tag{A-6}$$

$$\Gamma^0_{\mathrm{S^-}} = \frac{(\Gamma^0_{\mathrm{S}} - \Gamma^0_{\mathrm{X}})K_{\mathrm{H}}/10^{-\mathrm{pH}}}{1 + \frac{K_{\mathrm{H}}}{10^{-\mathrm{pH}}}(1 + C_f K_{\mathrm{Na}})}, \tag{A-7}$$

and

$$\Gamma^0_{\mathrm{SNa}} = \frac{(\Gamma^0_{\mathrm{S}} - \Gamma^0_{\mathrm{X}})C_f K_{\mathrm{Na}} K_{\mathrm{H}}/10^{-\mathrm{pH}}}{1 + \frac{K_{\mathrm{H}}}{10^{-\mathrm{pH}}}(1 + C_f K_{\mathrm{Na}})}. \tag{A-8}$$

All the charged sites that are not compensated in the Stern layer need to be compensated in the diffuse layer. Therefore, the fraction of counterions in the Stern layer is defined by the equations,

$$f = \frac{\Gamma^0_{\mathrm{SNa}}}{\Gamma^0_{\mathrm{SNa}} + \Gamma^0_{\mathrm{S^-}} + \Gamma^0_{\mathrm{X}}}, \tag{A-9}$$

and

$$f = f_M \left\{ \frac{C_f K_{\mathrm{Na}}}{f_M(1 + C_f K_{\mathrm{Na}}) + (1 - f_M)\left[1 + C_f K_{\mathrm{Na}} + \frac{10^{-\mathrm{pH}}}{K_H}\right]} \right\}, \tag{A-10}$$

where f_M designates the highest value of f reached at high salinities, i.e.,

$$f_M = \lim_{C_f \gg 1/K_{\mathrm{Na}}} f = 1 - \frac{\Gamma^0_{\mathrm{X}}}{\Gamma^0_S}. \tag{A-11}$$

The value of f_M is approximately 0.99 for kaolinite, 0.90 for illite, and 0.85 for smectite. At high pH values one has

$$f \approx f_M \left(\frac{C_f K_{\mathrm{Na}}}{1 + C_f K_{\mathrm{Na}}} \right). \tag{A-12}$$

Therefore, an increase of salinity is responsible for an increase of the partition coefficient f, which in turn is responsible for an increase of the magnitude of the quadrature conductivity (see Revil, 2012).

REFERENCES

Archie, G. E., 1942, The electrical resistivity log as an aid in determining some reservoir characteristics: Transactions of the American Institute of Mining, Metallurgical, and Petroleum Engineers, **146**, 54–62.

Avellaneda, M., and S. Torquato, 1991, Rigorous link between fluid permeability, electrical conductivity, and relaxation times for transport in porous media: Physics of Fluids A, **3**, 2529–2540, doi: 10.1063/1.858194.

Bear, J., 1988, Dynamics of fluids in porous media: Dover.

Bear, J., and Y. Bachmat, 1991, Introduction to modeling of transport phenomena in porous media: Kluwer Academic Publishers.

Bear, J., and A. H.-D. Cheng, 2010, Modeling groundwater flow and contaminant transport. Theory and applications of transport in porous media: Springer.

Bernabé, Y., and A. Revil, 1995, Pore-scale heterogeneity, energy dissipation and the transport properties of rocks: Geophysical Research Letters, **22**, 1529–1532, doi: 10.1029/95GL01418.

Bittar, M., J. Klein, R. Beste, G. Hu, M. Wu, J. Pitcher, C. Golla, G. Althoff, M. Sitka, V. Minosyan, and M. Paulk, 2009, A new azimuthal deep-reading resistivity tool for geosteering and advanced formation evaluation: SPE Reservoir Evaluation & Engineering, **12**, no. 2, 270–279, doi: 10.2118/109971-PA.

Clennell, B., 1997, Tortuosity: A guide through the maze, *in* M. A. Lovell, and P. K Harvey, eds., Developments in Petrophysics: Geological Society Special Publication 122, 299–344.

Deceuster, J., and O. Kaufmann, 2012, Improving the delineation of hydrocarbon-impacted soils and water through induced polarization (IP) tomographies: A field study at an industrial waste land: Journal of Contaminant Hydrology, **136–137**, 25–42, doi: 10.1016/j.jconhyd.2012.05.003.

Derkowski, A., and T. Bristow, 2012, On the problems of total specific surface area and cation exchange capacity measurements in organic-rich sedimentary rocks: Clays and Clay Minerals, **60**, no. 4, 348–362, doi: 10.1346/CCMN.2012.0600402.

Flores Orozco, A., K. H. Williams, P. E. Long, S. S. Hubbard, and A. Kemna, 2011, Using complex resistivity imaging to infer biogeochemical processes associated with bioremediation of an uranium-contaminated aquifer: Journal of Geophysical Research, **116**, G03001, doi: 10.1029/2010JG001591.

Helling, C. S., G. Chesters, and R. B. Corey, 1964, Contribution of organic matter and clay to soil cation exchange capacity as affected by the pH of the saturating solution: Soil Science Society of America Journal, **28**, 517–520, doi: 10.2136/sssaj1964.03615995002800040020x.

Johnson, D. L., T. J. Plona, and H. Kojima, 1986, Probing porous media with 1st sound, 2nd sound, 4th sound and 3rd sound, *in* R. Jayanth, J. Banavar, and K. W. Winkler, eds., Physics and Chemistry of Porous Media II, 243–277, American Institute of Physics.

Josh, M., L. Esteban, C. Delle Piane, J. Sarout, D. N. Dewhurst, and M. B. Clennell, 2012, Laboratory characterization of shale properties: Journal of Petroleum Science and Engineering, **88–89**, 107–124, doi: 10.1016/j.petrol.2012.01.023.

Kaiser, M., R. H. Ellerbrock, and H. H. Gerke, 2008, Cation exchange capacity and composition of soluble soil organic matter fractions: Soil Science Society of America Journal, **72**, 1278–1285, doi: 10.2136/sssaj2007.0340.

Leroy, P., and A. Revil, 2009, Spectral induced polarization of clays and clay-rocks: Journal of Geophysical Research, **114**, B10202, doi: 10.1029/2008JB006114.

Leroy, P., A. Revil, A. Kemna, P. Cosenza, and A. Ghorbani, 2008, Complex conductivity of water-saturated packs of glass beads: Journal of Colloid and Interface Science, **321**, 103–117, doi: 10.1016/j.jcis.2007.12.031.

Liang, B., J. Lehmann, D. Solomon, J. Kinyangi, J. Grossman, B. O'Neill, J. O. Skjemstad, J. Thies, F. J. Luizao, J. Petersen, and E. G. Neves, 2006, Black carbon increases cation exchange capacity in soils: Soil Science Society of America Journal, **70**, 1719–1730, doi: 10.2136/sssaj2005.0383.

Mandelson, K. S., and M. H. Cohen, 1982, The effect of grain anisotropy on the electrical properties of sedimentary rocks: Geophysics, **47**, 257–263, doi: 10.1190/1.1441332.

Olhoeft, G. R., 1986, Direct detection of hydrocarbon and organic chemicals with ground penetrating radar and complex resistivity: Proceedings of the National Water Wells Association Conference on Hydrocarbons and organic chemicals in ground water: Prevention, detection and restoration conference, 284–305.

Prasad, M., K. C. Mba, T. E. McEvoy, and M. L. Batzle, 2011, Maturity and impedance analysis or organic-rich shales: SPE Reservoir Evaluation and Engineering, **14**, 533–543, doi: 10.2118/123531-PA.

Pride, S. R., 1994, Governing equations for the coupled electromagnetics and acoustics of porous media: Physical Review B, **50**, 15678–15696, doi: 10.1103/PhysRevB.50.15678.

Revil, A., 2012, Spectral induced polarization of shaly sands: Influence of the electrical double layer: Water Resources Research, **48**, W02517.
Revil, A., 2013a, Effective conductivity and permittivity of unsaturated porous materials in the frequency range 1 mHz–1 GHz: Water Resources Research, **49**, doi: 10.1029/2012WR012700.
Revil, A., 2013b, On charge accumulations in heterogeneous porous materials under the influence of an electrical field: Geophysics, **78**, no. 4, D271–D291, doi: 10.1190/GEO2012-0503.1.
Revil, A., L. M. Cathles, S. Losh, and J. A. Nunn, 1998, Electrical conductivity in shaly sands with geophysical applications: Journal of Geophysical Research, **103**, 23,925–23,936, doi: 10.1029/98JB02125.
Revil, A., M. Darot, P. A. Pezard, and K. Becker, 1996, Electrical conduction in oceanic dikes, Hole 504B, *in* J. C. Alt, and H. Kinoshita, eds., Proceedings of the Ocean Drilling Program Science Research 148, 297–305.
Revil, A., J. D. Eppehimer, M. Skold, M. Karaoulis, L. Godinez, and M. Prasad, 2013, Low-frequency complex conductivity of sandy and clayey materials: Journal of Colloid and Interface Science, **398**, 193–209, doi: 10.1016/j.jcis.2013.01.015.
Revil, A., and N. Florsch, 2010, Determination of permeability from spectral induced polarization in granular media: Geophysical Journal International, **181**, 1480–1498.
Revil, A., and P. W. J. Glover, 1997, Theory of ionic surface electrical conduction in porous media: Physical Review B: Condensed Matter and Materials Physics, **55**, 1757–1773, doi: 10.1103/PhysRevB.55.1757.
Revil, A., K. Koch, and K. Holliger, 2012, Is it the grain size or the characteristic pore size that controls the induced polarization relaxation time of clean sands and sandstones?: Water Resources Research, **48**, W05602, doi: 10.1029/2011WR011561.
Revil, A., P. Leroy, and K. Titov, 2005, Characterization of transport properties of argillaceous sediments. Application to the Callovo-Oxfordian Argillite: Journal of Geophysical Research, **110**, B06202, doi: 10.1029/2004JB003442.
Revil, A., and M. Skold, 2011, Salinity dependence of spectral induced polarization in sands and sandstones: Geophysical Journal International, **187**, 813–824, doi: 10.1111/j.1365-246X.2011.05181.x.
Schmutz, M., A. Revil, P. Vaudelet, M. Batzle, P. Femenía Viñao, and D. D. Werkema, 2010, Influence of oil saturation upon spectral induced polarization of oil bearing sands: Geophysical Journal International, **183**, 211–224 doi: 10.1111/j.1365-246X.2010.04751.x.
Schwartz, N., and A. Furman, 2012, Spectral induced polarization signature of soil contaminated by organic pollutant: Experiment and modeling: Journal of Geophysical Research, **117**, B10203, doi: 10.1029/2012JB009543.
Sen, P. N., and P. A. Goode, 1992. Influence of temperature on electrical conductivity of shaly sands: Geophysics, **57**, 89–96, doi: 10.1190/1.1443191.
Sevostianova, E., B. Leinauer, and I. Sevostianov, 2010, Quantitative characterization of the microstructure of a porous material in the context of tortuosity: International Journal of Engineering Science, **48**, 1693–1701, doi: 10.1016/j.ijengsci.2010.06.017.
Skold, M., A. Revil, and P. Vaudelet, 2011, The pH dependence of spectral induced polarization of silica sands: Experiment and modeling: Geophysical Research Letters, **38**, L12304, doi: 10.1029/2011GL047748.
Slater, L., and D. P. Lesmes, 2002, Electrical-hydraulic relationships observed for unconsolidated sediments: Water Resources Research, **38**, 1213, doi: 10.1029/2001WR001075.
Vandenbroucke, M., and C. Largeau, 2007, Kerogen origin, evolution and structure: Organic Geochemistry, **38**, 719–833, doi: 10.1016/j.orggeochem.2007.01.001.
Vaudelet, P., A. Revil, M. Schmutz, M. Franceschi, and P. Begassat, 2011a, Changes in induced polarization associated with the sorption of sodium, lead, and zinc on silica sands: Journal of Colloid and Interface Science, **360**, 739–752, doi: 10.1016/j.jcis.2011.04.077.
Vaudelet, P., A. Revil, M. Schmutz, M. Franceschi, and P. Begassat, 2011b, Induced polarization signatures of cations exhibiting differential sorption behaviors in saturated sands: Water Resources Research, **47**, W02526, doi: 10.1029/2010WR009310.
Veeken, P. C. H., P. J. Legeydo, Y. A. Davidenko, E. O. Kudryavceva, S. A. Ivanov, and A. Chuvaev, 2009, Benefits of the induced polarization geoelectric method to hydrocarbon exploration, Geophysics, **74**, no. 2, B47–B59, doi: 10.1190/1.3076607.
Vinegar, H. J., and M. H. Waxman, 1984, Induced polarization of shaly sands: Geophysics, **49**, 1267–1287, doi: 10.1190/1.1441755.
Waxman, M. H., and L. J. M. Smits, 1968, Electrical conductivities in oil bearing shaly sands: SPE Journal, **8**, 107–122.
Weller, A., K. Breede, L. Slater, and S. Nordsiek, 2011, Effect of changing water salinity on complex conductivity spectra: Geophysics, **76**, no. 5, F315–F327, doi: 10.1190/geo2011-0072.1.
Weller, A., S. Nordsiek, and W. Debschütz, 2010, Estimating permeability of sandstone samples by nuclear magnetic resonance and spectral-induced polarization: Geophysics, **75**, no. 6, E215–E226, doi: 10.1190/1.3507304.
Weller, A., and L. Slater, 2012, Salinity dependence of complex conductivity of unconsolidated and consolidated materials: Comparisons with electrical double layer models: Geophysics, **77**, no. 5, D185–D198, doi: 10.1190/geo2012-0030.1.
Woodruff, W. F., and A. Revil, 2011, CEC-normalized clay-water sorption isotherm: Water Resources Research, **47**, W11502, doi: 10.1029/2011WR010919.
Zhang, J., and G. W. Scherer, 2012, Permeability of shale by the beam-bending method: International Journal of Rock Mechanics and Mining Sciences & Geomechanics Abstracts, **53**, 179–191, doi: 10.1016/j.ijrmms.2012.05.011.
Zhang, X., and M. A. Knackstedt, 1995, Direct simulation of electrical and hydraulic tortuosity in porous solids: Geophysical Research Letters, **22**, 2333–2336, doi: 10.1029/95GL02230.
Zimmermann, E., A. Kemna, J. Berwix, W. Glaas, H. M. Munch, and J. A. Huisman, 2008, A high-accuracy impedance spectrometer for measuring sediments with low polarizability: Measurement Science and Technology, **19**, 094010.
Zisser, N., A. Kemna, and G. Nover, 2010a, Dependence of spectral induced polarization response of sandstone on temperature and its relevance to permeability estimation: Journal of Geophysical Research, **115**, B09214, doi: 10.1029/2010JB007526.
Zisser, N., A. Kemna, and G. Nover, 2010b, Relationship between low-frequency electrical properties and hydraulic permeability of low-permeability sandstones: Geophysics, **75**, no. 3, E131–E141, doi: 10.1190/1.3413260.
Zisser, N., and G. Nover, 2009, Anisotropy of permeability and complex resistivity of tight sandstones subjected to hydrostatic pressure: Journal of Applied Geophysics, **68**, 356–370, doi: 10.1016/j.jappgeo.2009.02.010.